Hypoxia tolerance in the Norrin-deficient retina and the chronically hypoxic brain studied at single-cell resolution

Jacob S. Heng[a,b], Amir Rattner[a], Genevieve L. Stein-O'Brien[b,c], Briana L. Winer[b,c], Bryan W. Jones[d], Hilary J. Vernon[c], Loyal A. Goff[b,c], and Jeremy Nathans[a,b,e,f,1]

[a]Department of Molecular Biology and Genetics, Johns Hopkins University School of Medicine, Baltimore, MD 21205; [b]Department of Neuroscience, Johns Hopkins University School of Medicine, Baltimore, MD 21205; [c]McKusick–Nathans Institute of Genetic Medicine, Johns Hopkins University School of Medicine, Baltimore, MD 21205; [d]Moran Eye Center, University of Utah, Salt Lake City, UT 84132; [e]Department of Ophthalmology, Johns Hopkins University School of Medicine, Baltimore, MD 21205; and [f]Howard Hughes Medical Institute, Johns Hopkins University School of Medicine, Baltimore, MD 21205

The mammalian CNS is capable of tolerating chronic hypoxia, but cell type-specific responses to this stress have not been systematically characterized. In the Norrin KO (*Ndp*[KO]) mouse, a model of familial exudative vitreoretinopathy (FEVR), developmental hypovascularization of the retina produces chronic hypoxia of inner nuclear-layer (INL) neurons and Muller glia. We used single-cell RNA sequencing, untargeted metabolomics, and metabolite labeling from ^{13}C-glucose to compare WT and *Ndp*[KO] retinas. In *Ndp*[KO] retinas, we observe gene expression responses consistent with hypoxia in Muller glia and retinal neurons, and we find a metabolic shift that combines reduced flux through the TCA cycle with increased synthesis of serine, glycine, and glutathione. We also used single-cell RNA sequencing to compare the responses of individual cell types in *Ndp*[KO] retinas with those in the hypoxic cerebral cortex of mice that were housed for 1 week in a reduced oxygen environment (7.5% oxygen). In the hypoxic cerebral cortex, glial transcriptome responses most closely resemble the response of Muller glia in the *Ndp*[KO] retina. In both retina and brain, vascular endothelial cells activate a previously dormant tip cell gene expression program, which likely underlies the adaptive neoangiogenic response to chronic hypoxia. These analyses of retina and brain transcriptomes at single-cell resolution reveal both shared and cell type-specific changes in gene expression in response to chronic hypoxia, implying both shared and distinct cell type-specific physiologic responses.

Norrie disease | familial exudative vitreoretinopathy | single-cell RNA-seq | serine synthesis | metabolomics

The mammalian CNS is exquisitely sensitive to hypoxia. When combined with nutrient deprivation, hypoxia in the setting of acute ischemia causes rapid and irreversible cell loss in the brain and retina (1, 2). In contrast, mild to moderate hypoxia with continued nutrient delivery—as occurs at high altitude—can be tolerated for days to years (3, 4). In the laboratory, rodents can tolerate weeks to months in a hypoxia chamber with minimal long-term effects on brain morphology or neuronal function (5, 6). In the short term, hypoxia tolerance is likely mediated by metabolic suppression and reduced ion channel activity; in the longer term, it is likely mediated by changes in gene expression driven predominantly by hypoxia-inducible factors (HIFs) (7). These gene expression changes also protect against subsequent ischemia, a phenomenon known as hypoxic preconditioning (8). Previous work has hinted at CNS cell type-specific responses to hypoxia based, for example, on differences between cultured neurons and glia in their gene expression response to hypoxia (9) and on the activation of a latent angiogenic sprouting response by vascular endothelial cells (ECs) in the chronically hypoxic mouse brain (10). However, CNS cell type-specific responses to chronic hypoxia have not been examined in vivo on a genome-wide basis.

Hypoxia tolerance in the retina is likely to be a feature of familial exudative vitreoretinopathy (FEVR), an inherited disorder in which retinal blood vessels fail to develop normally (11). Approximately 50% of FEVR patients carry a loss-of-function mutation in one of the genes coding for the components of a canonical beta-catenin signaling pathway (11). In this system, the ligand Norrin [the protein product of the X-linked Norrie disease protein (*Ndp*) gene] is secreted by Muller glia and activates a complex of receptor, coreceptor, and coactivator (Frizzled4, LRP5, and TSPAN12, respectively) on the surface of retinal ECs, leading to the accumulation of the intracellular effector beta-catenin (CTNNB1) (12–14). We refer hereafter to this signaling system as Norrin/Frizzled4 signaling. The virtually identical cross-sectional anatomies of the human and mouse vasculatures made it possible to accurately model FEVR in mice with *Ndp*, *Fz4*, *Lrp5*, and *Tspan12* loss-of-function mutations (13–16). In both species, the choroidal circulation supplies the metabolic requirements of the cells in the outer nuclear layer, the rod and cone photoreceptors, whereas vessels on the vitreal

Significance

Chronic CNS hypoxia is a characteristic of diverse vascular disorders and environmental conditions. There is strong physiologic evidence that neurons and glia mount a protective response in the face of hypoxic stress. We used single-cell RNA sequencing and metabolic profiling to study the hypoxia responses of neurons and glia in the retina in a mouse model of familial exudative vitreoretinopathy, a developmental disorder in which retinal vascularization is incomplete. These responses were compared with those induced in the mouse cerebral cortex by a 1-week exposure to low atmospheric oxygen. These experiments reveal a distinctive set of genomic and metabolic responses in the hypoxic retina and a related set of genomic responses in the hypoxic cerebral cortex.

NEUROSCIENCE

surface of the retina together with the intraretinal vasculature, comprising two tiers of capillaries that flank the inner nuclear layer (INL), supply the metabolic requirements of the inner two layers of retinal neurons and glia. In FEVR patients (17) and mouse models (18, 19), reduced or absent Norrin/Frizzled4 signaling results in reduced or aborted development of the intraretinal and peripheral retinal blood vessels.

Despite the absence of intraretinal capillaries in murine retinas lacking Norrin/Frizzled4 signaling and the resulting hypoxia of the INL, the overall structure and cellularity of the mutant retina appear to be largely preserved, with minimal loss of INL cells over the first several months of life (20). It is likely that INL hypoxia in these retinas is substantially mitigated by loss of the blood–retina barrier (BRB), which allows small molecules, such as glucose, to diffuse into the INL (19). However, the function of the inner retina is severely affected: the b-wave of the electroretinogram, which arises from the summed responses of INL neurons to a flash of light, is greatly reduced, and there is no detectable transmission of visual information from rod and cone photoreceptors to retinal ganglion cells (RGCs) as measured by the optokinetic response (14, 15). Remarkably, when these retinas are placed in oxygenated Ringer's buffer, neurotransmission from the photoreceptors to the RGCs is restored within tens of minutes as evidenced by light-dependent RGC action potentials recorded with a multielectrode array (14). These observations hint at the existence of a reversible metabolic state that silences the hypoxic inner retina in vivo, and they suggest that studying the retinas of Norrin/Frizzled4-deficient mice could provide general insights into hypoxia tolerance in the CNS.

In this paper, we have explored the adaptations of murine *Ndp* KO (*Ndp^KO*) retinas to chronic hypoxia by (*i*) comparing the transcriptomes of WT and *Ndp^KO* retinas at single-cell resolution, (*ii*) comparing the metabolomes of WT and *Ndp^KO* retinas, and (*iii*) correlating these "omic" observations with histologic analyses. We have also analyzed, at single-cell resolution, the transcriptomes of the cerebral cortex from mice under normoxic conditions vs. mice exposed to 7 d of hypoxia (7.5% oxygen). These experiments reveal a distinctive set of genomic and metabolic responses in the hypoxic *Ndp^KO* retina and a related set of genomic responses in the hypoxic cerebral cortex.

Results

Minimal Morphologic Change in the *Ndp^KO* Retina. The absence of intraretinal capillaries in *Ndp^KO* retinas leads to chronic hypoxia that predominantly affects interneurons and glia that have their cell bodies (horizontal, bipolar, Muller, and nondisplaced amacrine cells) in the INL as demonstrated by the accumulation of pimonidazole (Hypoxyprobe) (Fig. 1*A*). The predominance of pimonidazole accumulation in the INL is consistent with the observations, in *Ndp^KO* mice, that (*i*) the pupillary light reflex (i.e., pupil constriction in response to light) is nearly normal, indicating
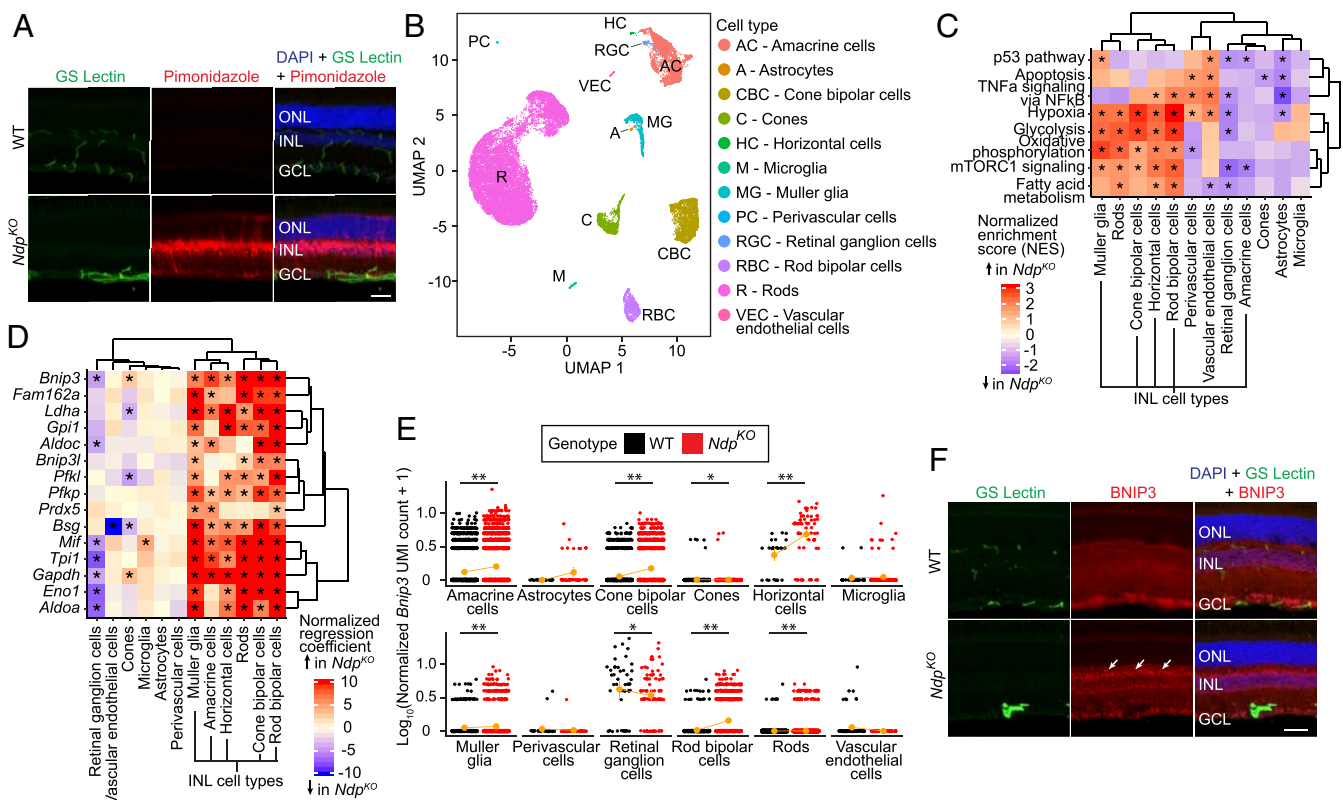
Fig. 1. scRNA-seq analysis of *Ndp^KO* retinas reveals transcriptional changes in INL cell types. (*A*) Immunofluorescence of adult WT and *Ndp^KO* retina cross-sections showing blood vessels (GS Lectin; green), hypoxic tissue (antipimonidazole; red), and nuclei (DAPI; blue). In this and other retina cross-sections, ganglion cell layer (GCL), INL, and outer nuclear layer (ONL) are shown. (Scale bar: 50 μm.) (*B*) UMAP plot showing different cell-type clusters in a merged dataset from duplicate samples of WT and *Ndp^KO* retinas. (*C*) Statistically significant MSigDB Hallmark pathways in three or more cell types on GSEA reveal pathways enriched in *Ndp^KO* over WT retinas across inner retinal cell types. *P value of <0.05. (*D*) Known hypoxia-inducible genes that are up-regulated in *Ndp^KO* compared with WT retinas in three or more cell types. *q value of <0.05. (*E*) Dot plots showing the log$_{10}$[number of *Bnip3* unique molecular identifiers (UMIs) + 1] for each cell for WT and *Ndp^KO* retinas plotted by cell type. Each orange dot and its associated vertical line represent the mean UMI count and its nonparametric bootstrap confidence interval, respectively, for each cell type of each genotype. The line connecting two oranges dots represents the trend in mean expression between the two genotypes for each cell type. *q value of <0.05 on differential gene expression testing; **q value of <0.01 on differential gene expression testing. (*F*) Immunofluorescence of adult WT and *Ndp^KO* retina cross-sections showing blood vessels (GS Lectin; green), BNIP3 (red), and nuclei (DAPI; blue). BNIP3 immunofluorescence is more intense in the *Ndp^KO* INL (indicated by white arrows) compared with the WT INL. (Scale bar: 50 μm.)

that intrinsically photoreceptive RGCs are functional, and that (*ii*) the a-wave of the electroretinogram is unaffected, indicating that photoreceptors are functional (14, 15).

To assess the structure of the Ndp^{KO} retina in greater detail, we compared 2-mo-old Ndp^{KO} and WT retinas by transmission EM (TEM) and by immunostaining. By TEM, the presence of ribbon synapses and the density and overall structure of the neuropil in the outer plexiform layer (OPL) and inner plexiform layer (IPL) were indistinguishable between Ndp^{KO} and WT retinas, as was the appearance of nuclei in the INL (*SI Appendix*, Fig. S1*A*). Immunostaining for markers in the INL and its adjacent plexiform layers generally showed indistinguishable patterns of staining in Ndp^{KO} and WT retinas. These include vesicular glutamate transporter-1, a presynaptic marker of glutamatergic synapses (*SI Appendix*, Fig. S1*B*); postsynaptic density protein 95, a postsynaptic marker (*SI Appendix*, Fig. S1*B*); and markers for horizontal cells (Neurofilament-H and Calbindin), RGC axons (Neurofilament-H), cholinergic amacrine cells, and various amacrine and RGC subsets (Calretinin) (*SI Appendix*, Fig. S1*C*). A marker for rod bipolar cells (PKC-alpha) showed the same pattern but was less intense in Ndp^{KO} compared with WT retinas (*SI Appendix*, Fig. S1*C*). Vascular markers (GS-lectin for ECs and Aquaporin-4 for EC-associated Muller processes) showed the expected absence of intraretinal capillaries in Ndp^{KO} retinas (*SI Appendix*, Fig. S1*C*).

The essentially normal neuronal structure in the Ndp^{KO} retina, as seen by TEM and immunostaining, is consistent with the earlier observation of a rapid recovery of neurotransmission across the inner retina when Ndp^{KO} retinas are provided with oxygen and glucose ex vivo (14). Taken together, the data suggest that the dormancy of INL neurons in Ndp^{KO} retinas likely arises from a reversible change in metabolic state.

Single-Cell RNA-seq of Ndp^{KO} Retinas Reveals both Shared and Cell Type-Specific Gene Expression Changes. Using a droplet-based single-cell RNA-seq (scRNA-seq) platform (10× Genomics), we characterized 32,825 dissociated retinal cells from 8-wk-old Ndp^{KO} mice and WT littermate controls. The data were derived from two independent samples per genotype. All 12 major retinal cell types were readily identified based on known markers (*SI Appendix*, Fig. S2 *B* and *C*) and showed distinct clusters on a Uniform Manifold Approximation and Projection (UMAP) (21) plot (Fig. 1*B*); 1,133 presumed multiplets were excluded from subsequent analyses. When cells from Ndp^{KO} and WT retinas were visualized separately, they showed very similar clustering behavior (*SI Appendix*, Fig. S2*A*). Cross-sample normalization was performed via mean scaling of the raw transcript copies per cell in each cell type independently. Although a previous study suggested inflammation as a consequence of the loss of BRB integrity in Ndp^{KO} retinas (22), we did not observe infiltrating immune cells by scRNA-seq.

Using Monocle2 (23, 24), we next generated a negative binomial regression model that included parameters for genotype, cell type, sequencing depth, and batch effects. This permitted the calculation of a *z*-scored genotype regression coefficient for each gene and the identification of differentially expressed genes on a per cell type basis. To identify gene sets with differential representation in WT vs. Ndp^{KO} datasets, genes were ranked based on the *z*-scored genotype regression coefficient for each gene in each cell type, and this ranking was used for a preranked gene set enrichment analysis (GSEA) analysis (25). This preranked GSEA performed with the "Hallmark" gene sets curated by the Molecular Signatures DataBase (MSigDB) (26) identified gene sets, including the "Hypoxia" gene set, that were positively enriched in Ndp^{KO} retinas in multiple INL cell types, including Muller glia, rod bipolar, cone bipolar cells, and horizontal cells (Fig. 1*C*).

The cell type-specific gene expression changes (Monocle2 test; *q* value ≤ 0.05) observed by scRNA-seq are consistent with the hypothesis that the INL is the site of the greatest hypoxic stress in the Ndp^{KO} retina. A subset of known hypoxia-induced genes

from the Hypoxia gene set (MSigDB) was significantly up-regulated in most INL cell types (Fig. 1*D* and *SI Appendix*, Fig. S2*D*), consistent with the pimonidazole labeling experiment. Interestingly, many of the same transcripts were also enriched in rods but not enriched in cones. One possible explanation for the different responses of rods and cones is that cones are intrinsically less energy consuming than rods. Another more speculative possibility is that, based on the steep decline in oxygen concentration between retinal pigment epithelium (RPE; ~70 mmHg) and the OPL (~10 mmHg) (27), the loss of intraretinal vasculature might produce a greater hypoxic stress in those rods with nuclei closer to the INL compared with cones, which have their nuclei closer to the RPE where the oxygen concentration is higher.

Many of the differentially expressed genes in INL cells in the hypoxic Ndp^{KO} retina are targets of HIFs. Two examples shown in detail are *Bnip3* and *Bsg*. *Bnip3* is up-regulated approximately twofold in all INL cell types by scRNA-seq (Fig. 1*E*), consistent with the modest elevation in BNIP3 immunostaining intensity in the INL in Ndp^{KO} retinas (Fig. 1*F*). *Bnip3* up-regulation has been shown to mitigate oxidative stress in the context of hypoxia by mediating mitophagy (28). *Bsg*, another HIF-regulated gene, is up-regulated approximately twofold in INL cells in Ndp^{KO} retinas but is paradoxically down-regulated >10-fold in ECs (*SI Appendix*, Fig. S2 *E* and *F*). *Bsg* codes for Basigin (CD147), a widely expressed multifunctional transmembrane protein that associates with and directs the trafficking of integral membrane monocarboxylate transporters to promote glycolysis in hypoxia (29, 30). However, the presence of T cell factor/lymphocyte enhancer-binding factor (TCF/LEF) binding motifs in accessible chromatin regions upstream of the *Bsg* promoter in CNS ECs (31) suggests that *Bsg* may also be a beta-catenin target gene required for the maturation of cell–cell junctions in CNS ECs (32). Its down-regulation in Ndp^{KO} ECs is consistent with a loss of beta-catenin signaling in ECs in the absence of *Ndp*.

In addition to *Bnip3* and *Bsg* (described above), the glycolytic enzyme genes *Aldoa*, *Aldoc*, *Ldha*, *Pfkp*, *Pfkl*, *Gapdh*, *Tpi1*, *Eno1*, and *Gpi1* are all targets of HIF regulation (33) and are significantly up-regulated in INL cells in Ndp^{KO} retinas (Fig. 1*D*). *Prdx5*, which is up-regulated in a subset of INL cells, is a known hypoxia-inducible gene (34) that codes for Peroxiredoxin-5, an enzyme that confers antioxidant protection by reducing hydrogen peroxide (35). Taken together, these gene expression changes are consistent with a model in which transcriptional changes during hypoxia, driven primarily by HIFs, promote glycolysis and/or inhibit the mitochondrial respiratory chain, which together minimize the production of reactive oxygen species (ROS) (36). Additional defenses against ROS are provided by up-regulation of genes, such as *Prdx5*.

Metabolic Changes in the Ndp^{KO} Retina Are Centered Around Glutathione and One-Carbon Metabolism. As many of the transcripts that are enriched in Ndp^{KO} retinas are linked to metabolism, we performed an untargeted survey of the metabolome using capillary electrophoresis (CE)–TOF MS on ionic metabolites isolated from whole Ndp^{KO} and WT retinas (Dataset S1). Based on six independent samples per genotype, CE-TOF MS identified dozens of metabolites that showed consistent changes in abundances (as measured by the CE-TOF MS relative peak areas) between Ndp^{KO} and WT retinas (Fig. 2 *A* and *C* and *SI Appendix*, Fig. S3 *A* and *E* and Table S1). By principal component analysis (PCA) of the untransformed CE-TOF MS relative peak areas across metabolites, the Ndp^{KO} and WT retina metabolomes are clearly distinct (*SI Appendix*, Fig. S3*B*).

The hypoxic state of the INL and the marked reduction in inner retinal neurotransmission might reasonably suggest a reduction in ATP levels and a reduction in the ATP/ADP ratio in the INL. Surprisingly, these values for the entire retina were essentially identical in Ndp^{KO} vs. WT retinas (*SI Appendix*, Fig. S3*C* and Table S1). Classical microchemical studies of ATP and ADP content in different retinal layers found that the ATP content of the INL represents ~28% of total retina ATP (37).
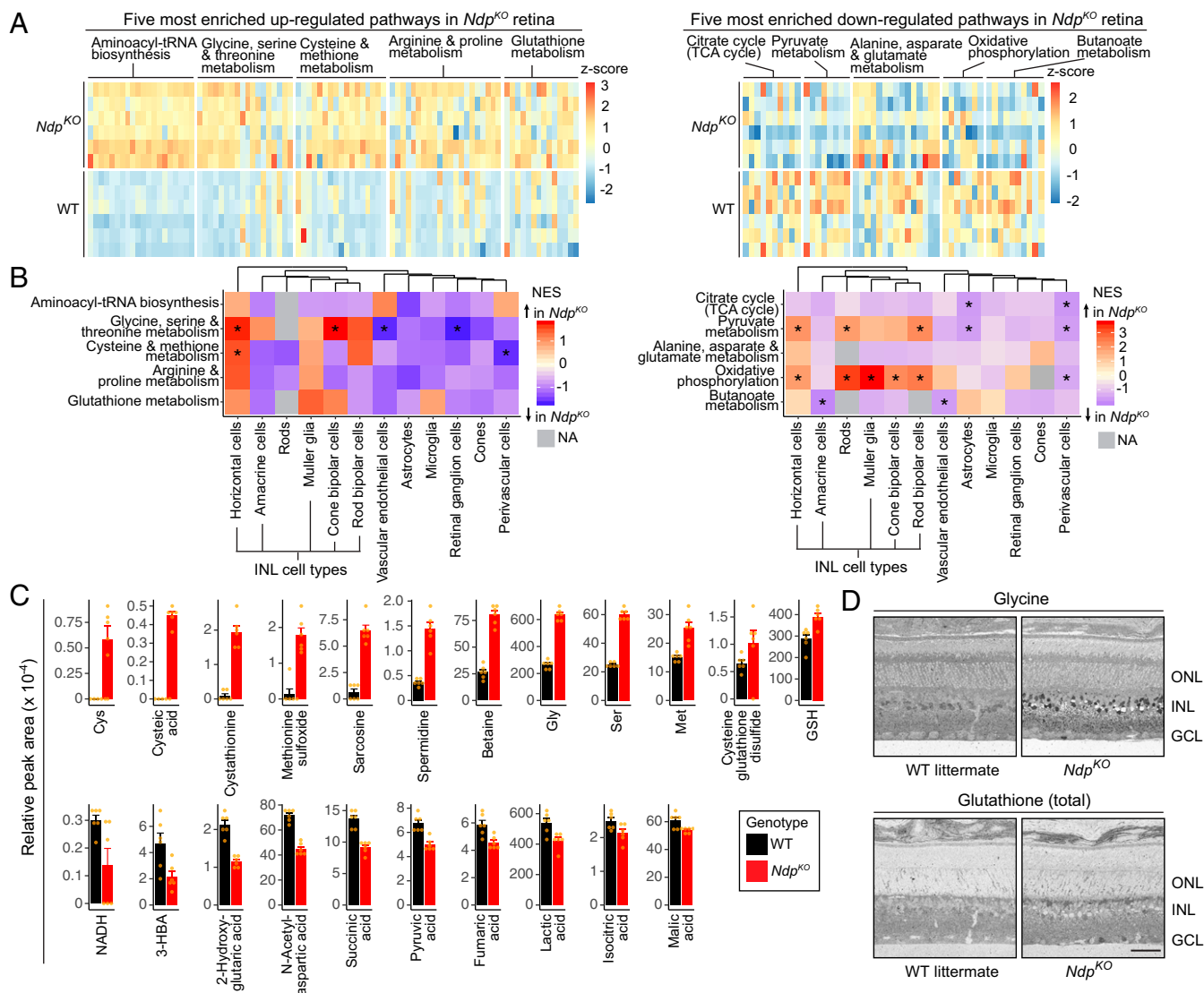
Fig. 2. Untargeted metabolic profiling of WT and Ndp^{KO} retinas reveals metabolic changes centered around glutathione and one-carbon metabolism. (*A*) Heat maps showing individual metabolites in the top five up-regulated in Ndp^{KO} (*Left*) and top five down-regulated in Ndp^{KO} (*Right*) metabolic pathways as determined by overrepresentation analysis. Each row represents an independent retina sample, and each column represents a metabolite. (*B*) Heat maps showing enrichment scores for each cell type in GSEA for the same 10 Ndp^{KO}-enriched pathways shown in *A*. NA, nonapplicable (gray), indicating that GSEA could not be performed due to the low signal for the relevant pathway genes in a particular cell type; NES, normalized enrichment score. *P value of <0.05. (*C*) Bar plots showing relative MS peak areas for representative metabolites in the Ndp^{KO}-enriched metabolic pathways listed in *A*. Error bars represent the SEM. Orange dots represent individual samples. (*D*) Immunogold staining with antibodies raised against metabolite-hapten conjugates followed by silver intensification. Elevated levels of glycine and total glutathione in Ndp^{KO} retinas were mainly localized to the INL. GCL, ganglion cell layer; ONL, outer nuclear layer. (Scale bar: 50 μm.)

Thus, even a relatively modest (e.g., 30%) reduction in the INL ATP level or in the INL ATP/ADP ratio should have produced a detectable reduction (~10%) in the whole-retina analysis. In contrast, NADH levels and the NADH/NAD$^+$ ratio were roughly halved in the Ndp^{KO} retina (*SI Appendix,* Fig. S3C), consistent with oxidative stress in the Ndp^{KO} INL and/or decreased entry of pyruvate into the TCA cycle via acetyl-CoA.

An overrepresentation analysis, implemented with the MetaboAnalystR software (38), identified statistically significant up- and down-regulated metabolic pathways in Ndp^{KO} vs. WT retinas. Pathways that were most significantly up-regulated are centered around glutathione and one-carbon metabolism, including glycine, serine, threonine, cysteine, and methionine metabolism (Fig. 2 *A, Left* and *C* and *SI Appendix,* Fig. S3D, *Left*). There were marked increases in cystathionine and cysteine in the Ndp^{KO} retina (Fig. 2C), consistent with increased activity in the transsulfuration pathway. Pathways that were significantly down-regulated include the TCA cycle and the mitochondrial electron transport chain, which are known to be inhibited in chronic hypoxia (Fig. 2 *A, Right* and *C* and *SI Appendix,* Fig. S3D, *Right*) (36). These metabolite changes correlate broadly with gene expression changes as determined by GSEA of the scRNA-seq data from Ndp^{KO} vs. WT INL cell types (Fig. 2B), especially in glycine, serine, and threonine metabolism. However, some genes involved in oxidative phosphorylation are up-regulated in Ndp^{KO} retinas (Fig. 2B, *Right* and *SI Appendix,* Table S2), despite some metabolic intermediates in oxidative phosphorylation being down-regulated (Fig. 2C and *SI Appendix,* Table S1). This apparent discrepancy most likely reflects hypoxia-induced changes in the subunit composition of the mitochondrial respiratory chain complexes (39–41). More generally, apparent discrepancies between transcriptome and metabolome changes in Ndp^{KO} vs. WT

retinas could represent homeostatic gene regulatory responses to altered levels of particular metabolites.

To localize and independently assess changes in metabolite levels, we performed computational molecular phenotyping (CMP) (42, 43). CMP utilizes immunogold staining of resin-embedded tissues with antibodies raised against hapten-metabolite conjugates followed by silver intensification. In general agreement with the metabolomics data (Fig. 2C), CMP showed increases in glycine and glutathione in the INL (Fig. 2D).

^{13}C Metabolite Labeling Reveals the Requirement for de Novo Serine Synthesis in the Ndp^{KO} Retina.

Since the Ndp^{KO} vs. WT retina metabolomics analysis described above revealed differential signals in pathways linked to glucose metabolism, we performed in vivo metabolite labeling with uniformly labeled ^{13}C-glucose by injecting Ndp^{KO} and WT mice i.p. with 2 g/kg ^{13}C-glucose and harvesting retinas 45 min later (four groups of mice per geno-

type) (Dataset S2). In Fig. 3 and *SI Appendix*, Fig. S4, we refer to chemical species observed on MS as "M + X" to indicate X additional mass units beyond the nonlabeled species. Since the natural isotope of carbon is ^{12}C, each ^{13}C adds one mass unit.

As a preliminary experiment, we injected Ndp^{KO} and WT mice i.p. with 2-(N-(7-nitrobenz-2-oxa-1,3-diazol-4-yl)amino)-2-deoxyglucose (2-NBDG), a fluorescent glucose analog, and found that, despite the hypovascularization of the Ndp^{KO} retina, 2-NBDG was present in the INL of the Ndp^{KO} retina at a higher level compared with the WT retina (*SI Appendix*, Fig. S4A). This apparent paradox is likely explained by the loss of vascular barrier function in the Ndp^{KO} retina, which allows rapid equilibration of low-molecular weight compounds between serum and the extravascular space (18). Interestingly, the scRNA-seq data showed that the genes coding for hexokinase (*Hk1* and *Hk2*), the enzyme responsible for the first enzymatic transformation of glucose (to glucose 6-phosphate) after cellular uptake, are down-regulated in photoreceptors but
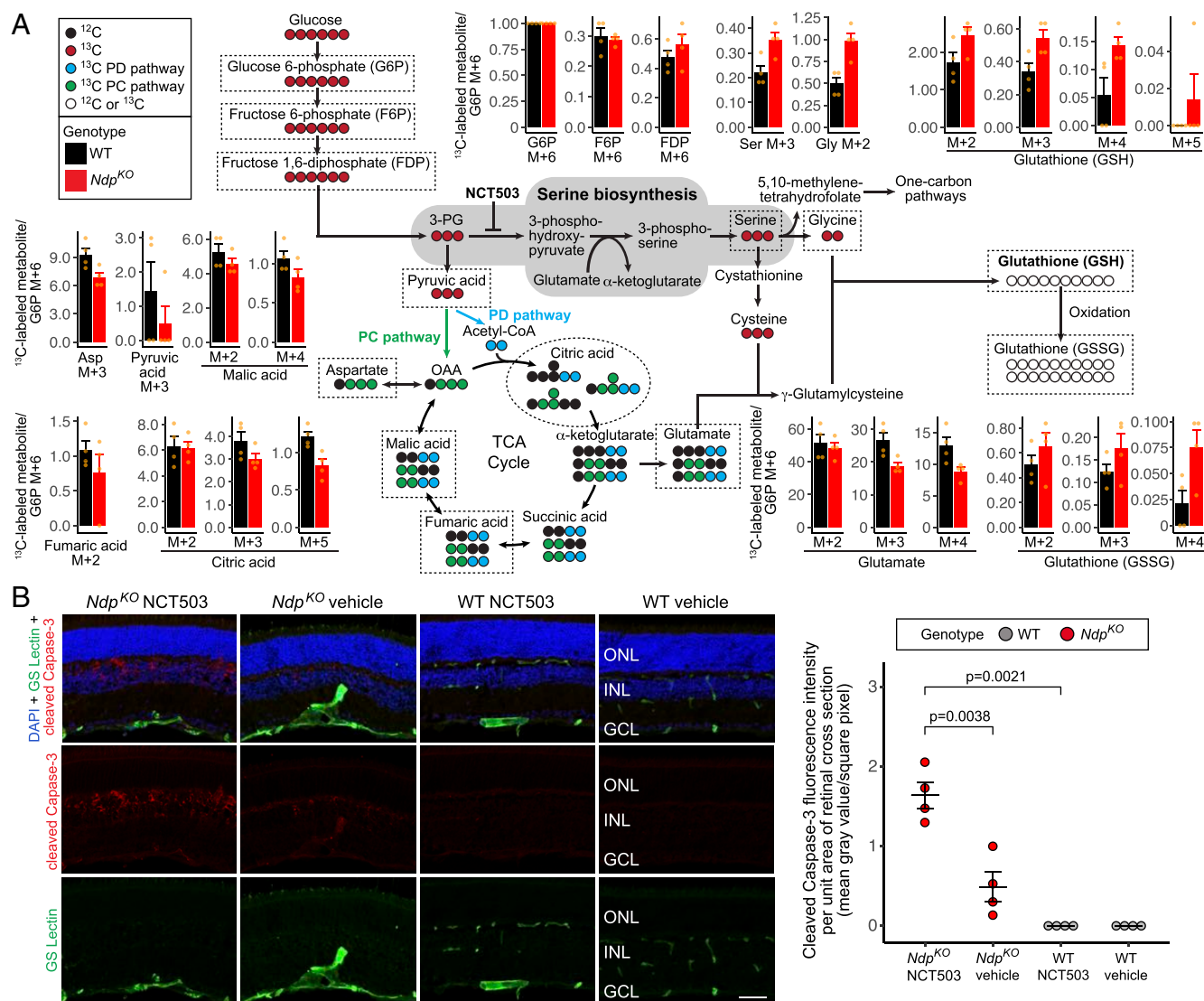

Fig. 3. Metabolic flux analysis and pharmacological inhibition reveal enhanced de novo serine biosynthesis in Ndp^{KO} retinas in vivo. (A) Schematic showing the fates of ^{13}C atoms from uniformly labeled ^{13}C-glucose. For metabolites enclosed in dashed lines in the schematic, the surrounding bar plots show the mean ratios of the measured abundances of ^{13}C-labeled metabolites to the abundance of ^{13}C-glucose 6-phosphate (M + 6) for WT and Ndp^{KO} retinas. Orange dots represent individual samples. PC pathway, pyruvate carboxylase pathway; PD pathway, pyruvate dehydrogenase pathway. (B) The effect on apoptotic pathway activation of systemic treatment with NCT503 (an inhibitor of PHGDH; 40 mg/kg vs. vehicle, daily i.p. injections for 12 d). (Left) Representative images of immunofluorescence of retina cross-sections showing blood vessels (GS Lectin; green), cleaved Caspase-3 (red), and nuclei (DAPI; blue). (Right) Quantification of cleaved Capase-3 immunofluorescence of two random whole-retina cross-sections per eye. Horizontal bars represent the mean and the SEM. GCL, ganglion cell layer; ONL, outer nuclear layer.

up-regulated in INL cell types in the Ndp^{KO} retina (*SI Appendix*, Fig. S4B). Overall, however, the uptake efficiency of ^{13}C-glucose into retinal cells seems to be similar for WT and Ndp^{KO} mice as judged by the levels of glucose 6-phosphate M + 6 (*SI Appendix*, Fig. S4C), which constituted 16–26% of total glucose 6-phosphate in the samples (*SI Appendix*, Fig. S4D). For each sample in the ^{13}C experiment, the abundances of labeled metabolites were divided by the level of glucose 6-phosphate (M + 6) to account for differences in ^{13}C-glucose uptake (Dataset S3). The overall pattern of ^{13}C-labeled metabolites showed a clear distinction between Ndp^{KO} and WT samples by PCA (*SI Appendix*, Fig. S4E).

Despite the dilution of ^{13}C-glucose throughout the body, the small amount of retinal tissue, and the relatively brief labeling period, there was detectable ^{13}C incorporation into multiple metabolites across glycolysis, the TCA cycle, the pentose phosphate pathway, and glutathione metabolism (Fig. 3A and *SI Appendix*, Fig. S4F). Ndp^{KO} retinas showed decreases in glutamate and in multiple ^{13}C-labeled TCA cycle metabolites (Fig. 3A and *SI Appendix*, Table S3). In contrast, serine M + 3 and glycine M + 2 were increased in the Ndp^{KO} samples, suggesting an increase in glucose flux into de novo serine synthesis and serine metabolism (Fig. 3A). Although transcripts coding for the rate-limiting enzyme in de novo serine synthesis, phosphoglycerate dehydrogenase (PHGDH), were only detected at low abundance on scRNA-seq and show no significant difference in INL cell types, immunofluorescence showed an apparent increase in PHGDH protein in Muller glia in Ndp^{KO} retinas (compare staining intensity of radial processes in *SI Appendix*, Fig. S4H). The increase

in ^{13}C-labeled serine and glycine was accompanied by an increase in ^{13}C-labeled reduced and oxidized glutathione (GSH and GSSG, respectively) (Fig. 3A), which is consistent with the increase in steady-state serine, glycine, and glutathione seen in the non-isotopic metabolomics data (Fig. 2 C and D). Increased de novo serine synthesis is likely to contribute to increased glutathione synthesis through the transsulfuration pathway as evidenced by the marked increases in cystathionine and cysteine in the Ndp^{KO} retina (Fig. 2C).

De novo serine synthesis is an important source of glutathione (Fig. 3A), a major cellular antioxidant. In cultured Muller glia, disruption of de novo serine synthesis through inhibition of PHGDH reduces glutathione levels and increases cellular damage under mild oxidative stress (44). We, therefore, hypothesized that inhibiting de novo serine synthesis could exacerbate cellular oxidative stress specifically in the hypoxic Ndp^{KO} inner retina. To test this hypothesis, we injected Ndp^{KO} mice and their WT littermates i.p. with 40 mg/kg NCT503 or vehicle control daily for 12 consecutive days and then analyzed their retinas for cleaved Caspase-3, a marker of apoptosis. NCT503 is a well-characterized small molecule inhibitor of PHGDH (45). As seen in Fig. 3B, WT retinas show undetectable levels of cleaved Caspase-3, irrespective of whether they have been treated with vehicle or NCT503, whereas Ndp^{KO} retinas show low levels of cleaved Caspase-3 after vehicle injection and high levels of cleaved Caspase-3 after NCT503 injection. In both cases, the cleaved Caspase-3 was confined to the INL, and it was enriched in regions of cellular disorganization that resemble the cystoid lesions that
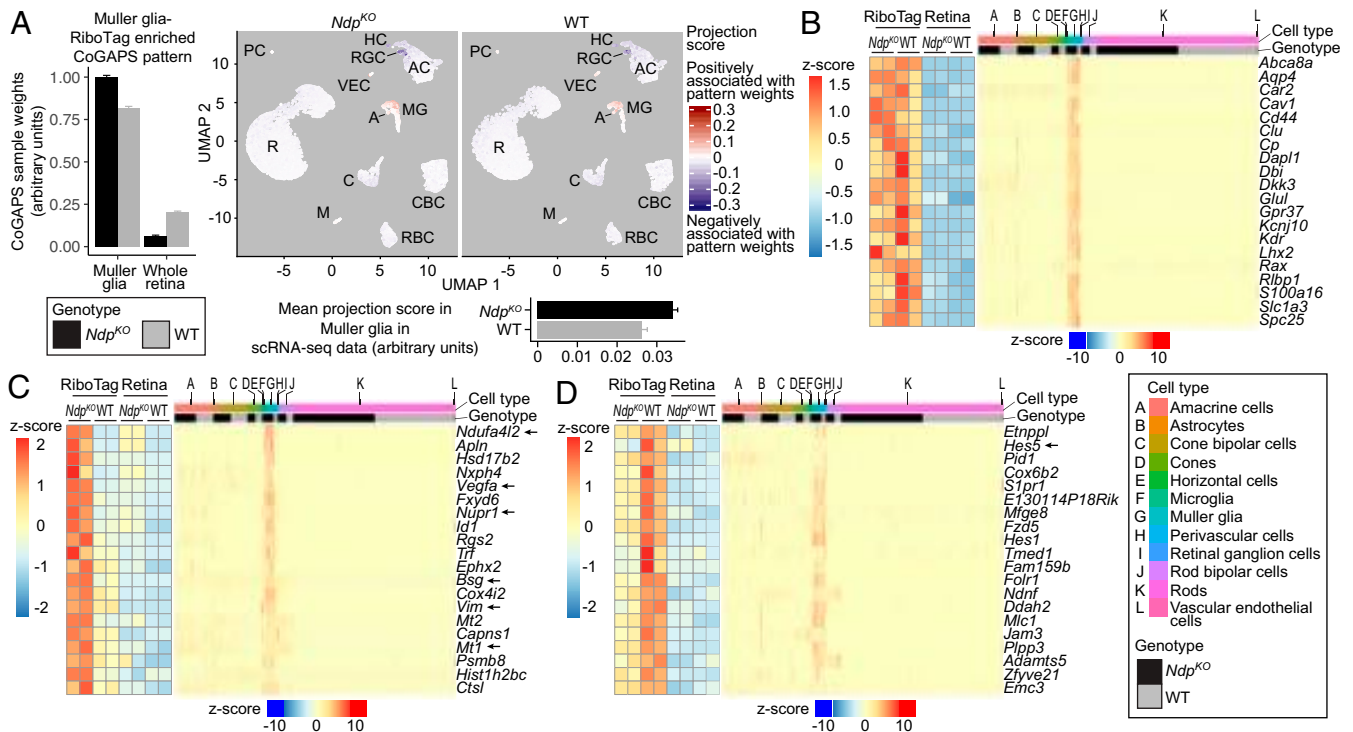
Fig. 4. RiboTag and scRNA-seq analysis of Muller glia-enriched transcripts in WT and Ndp^{KO} retinas converge on a common set of differentially expressed genes. (*A, Left*) CoGAPS sample weights of the Muller glia-RiboTag–enriched pattern for Muller glia-RiboTag and whole-retina samples. (*A, Upper Right*) Projections of the Muller glia-RiboTag–enriched pattern into WT and Ndp^{KO} scRNA-seq datasets visualized on UMAP plots. (*A, Lower Right*) Mean projection scores of the Muller glia-RiboTag–enriched pattern in Ndp^{KO} and WT Muller glia clusters of the scRNA-seq datasets. Error bars represent the SEM. (*B*) Expression of Muller glia-enriched transcripts in Muller glia-RiboTag vs. whole-retina RNA-seq (*Left*) and in scRNA-seq (*Right*). In *B–D*, each cell in the scRNA-seq dataset is represented by a point along the horizontal axis, and the regions of the plot corresponding to different cell types and to WT vs. Ndp^{KO} are color coded across the top. (*C*) Analysis as in *B*, except that *C* shows Muller glia-enriched transcripts that were also up-regulated in Ndp^{KO} retinas in the Muller glia-RiboTag RNA-seq (*Left*) and scRNA-seq datasets (*Right*). (*D*) Analysis as in *B*, except that *D* shows Muller glia-enriched transcripts that were also down-regulated in Ndp^{KO} retinas in the Muller glia-RiboTag RNA-seq (*Left*) and scRNA-seq datasets (*Right*). As seen in *B–D*, among retinal cells, retinal astrocytes bear the closest resemblance to Muller glia as judged by their patterns of transcript abundances. A, astrocyte; AC, amacrine cell; C, cone; CBC, cone bipolar cell; HC, horizontal cell; M, microglia; MG, Muller glia; PC, perivascular cell; R, rod; RBC, rod bipolar cell; VEC, vascular endothelial cell.

develop in the INL in older Ndp^{KO} retinas (22), suggesting that NCT503 may accelerate what would otherwise be a slower degenerative process. These data are consistent with a model in which a combination of hypoxia and reduced de novo serine synthesis produces a level of cellular stress that is sufficient to activate Caspase-3 cleavage.

Muller Glia in the Ndp^{KO} Retina Exhibit Distinct Transcriptional Changes. In the Ndp^{KO} retina, *Vegfa* transcripts are selectively up-regulated in Muller glia (18). To verify additional transcriptome changes in Ndp^{KO} Muller glia identified with scRNA-seq, a Muller glia-specific CreER transgene (GLAST-CreER) (46) was crossed to RiboTag mice (47) to activate production of an epitope-tagged ribosomal protein in a Cre recombinase-dependent manner in Muller glia. This allowed us to immunoaffinity purify polyribosomes from Muller glia for RNA-seq. We will refer to the resulting RNA-seq datasets as "Muller glia-RiboTag" datasets.

Duplicate Ndp^{KO} and WT RNA-seq datasets from whole retina and from Muller glia-RiboTag–purified transcripts were appropriately clustered (*SI Appendix*, Fig. S5A). To identify patterns in the Muller glia-enriched and whole-retina RNA-seq datasets in an unbiased fashion, we used the Coordinated Gene Activity in Pattern Sets (CoGAPS) algorithm (48). CoGAPS decomposes gene expression into a set of patterns that quantify the association of each sample with a vector of relative gene expression changes. Unlike clustering methods, CoGAPS allows a gene to contribute to more than one pattern, which more effectively captures the complexity of gene expression patterns associated with specific cell types and physiologic perturbations.

CoGAPS identified a pattern with higher weights in Muller glia-RiboTag samples compared with the whole-retina samples (Fig. 4A, *Left*). When projected into the scRNA-seq dataset using the projectR software (49), this Muller glia-RiboTag–enriched CoGAPS pattern showed the highest projection scores in the Muller glia cluster for both Ndp^{KO} and WT scRNA-seq datasets, consistent with the expectation that it reflects a Muller glial transcriptional signature. Indeed, known Muller glia markers (50) were found to specifically have high gene weights for this pattern and also showed significant enrichment in both Muller glia-Ribotag samples and Muller glia scRNA-seq data for Ndp^{KO} and WT samples (Fig. 4B). In addition, this pattern showed higher weights in the Ndp^{KO} compared with the WT Muller glia-RiboTag samples (Fig. 4A) and higher projection scores for Ndp^{KO} than WT Muller glia in the scRNA-seq data (Fig. 4C), implying that this CoGAPS pattern also includes a hypoxia response signature.

We next intersected statistically significant (q value ≤ 0.05) gene expression changes in Muller glia from the RiboTag and scRNA-seq datasets. Using as thresholds a specificity score of ≥ 0.4 (Monocle2) for Muller glia in the scRNA-seq dataset and twofold enrichment for the Muller glia-RiboTag–enriched dataset, there were 27 up- and 65 down-regulated Muller glia-enriched genes in the intersection of the two datasets (*SI Appendix*, Fig. S5 B and C and Table S4); 24 of 27 up-regulated Muller enriched genes are also specific to the Muller glia CoGAPS pattern described above. Twenty examples each from the up- and down-regulated Muller glia-enriched genes are shown in Fig. 4 C and D. For five differentially regulated genes—*Vegfa*, *Ndufa4l2*, *Bsg*, *Mt1*, and *Hes1*—in situ hybridization to sections of Ndp^{KO} and WT retinas confirmed the changes in transcript abundance in the INL in Ndp^{KO} retinas (Fig. 5 A and B and *SI Appendix*, Fig. S2 E and F for *Bsg*). Immunostaining confirmed the increased abundances of the proteins encoded by the up-regulated genes *Nupr1* and *Vim* (Fig. 5C). *Gfap* was identified as a Muller-enriched up-regulated gene in the scRNA-seq analysis (*SI Appendix*, Fig. S5E) but did not pass the enrichment threshold for RiboTag analysis. Immunostaining confirmed the increased abundance of GFAP in Muller glia (*SI Appendix*, Fig. S5F), suggesting that the scRNA-seq analysis may be able to better discern cell type-specific gene expression changes compared with the RiboTag analysis.

The Muller glia genes that are up-regulated in Ndp^{KO} retinas code for a functionally diverse set of proteins. *Ndufa4l2* codes for a hypoxia-induced mitochondrial protein that inhibits Complex I and reduces oxygen consumption (41). *Mt1* codes for Metallothionien-1, an intracellular metal chelator, that is induced by diverse cellular stresses, including hypoxia (51). *Nupr1* codes for a nuclear protein that protects against DNA damage-induced cell death in hypoxia (52). *Vim* and *Gfap* code for Vimentin and Glial Fibrillary Acidic Protein, respectively, which are intermediate filaments up-regulated in Muller glia in response to a variety of retinal insults, and they are postulated to protect against mechanical stress (53). *Hes1* is downstream of Notch signaling, and it is down-regulated in the INL in Ndp^{KO} retinas. Notch signaling has been implicated in generating and maintaining glial identity in postmitotic Muller glia (54).

A Comparison of Transcriptional Changes in Ndp^{KO} Retinas and in Chronic Brain Hypoxia. Since the retina is part of the CNS, it was of interest to compare the gene expression changes identified in the hypoxic Ndp^{KO} INL with those induced by a similar stress in the brain. For this comparison, chronic global hypoxia in the brain—induced by housing mice for up to 7 d in an atmosphere of 7.5% oxygen—is presumed to be similar to the hypoxic Ndp^{KO} INL, since the former does not reduce the exchange of molecules other than oxygen.

In an initial set of experiments, cages housing 8- to 10-wk-old C57BL/6J male mice were maintained in room air (~21% oxygen) or were placed in 7.5% oxygen for either 48 h or 7 d before harvesting their brains for bulk RNA-seq. CoGAPS analysis revealed two distinct patterns of gene expression responses to hypoxia (Fig. 6A and Dataset S4). The first pattern was characterized by an increase in transcript abundance between 0 and 48 h of hypoxia followed by a plateau or a decrease between 48 h and 7 d of hypoxia. The second pattern was characterized by a continuous increase in transcript abundance from 0 h through 7 d of hypoxia. Gene expression changes in response to 7 d of hypoxia that were not seen with 48 h of hypoxia likely represent the response to chronic hypoxia, suggesting that 7 d was sufficient to induce a chronically hypoxic state in the brain.

To characterize cell type-specific transcriptional changes in the chronically hypoxic brain, we performed scRNA-seq on 7,925 dissociated cells from cerebral cortices from 8- to 10-wk-old C57BL/6J male mice housed in room air or in 7.5% oxygen for 7 d, conditions that are referred to hereafter as normoxia and hypoxia, respectively. Based on known markers, we identified all of the major cortical cell types with similar yields in the normoxic and hypoxic samples (Fig. 6B and *SI Appendix*, Fig. S6 A, C, and D). *SI Appendix*, Fig. S6B shows that, in contrast to the interspersion of GABAergic and glutamatergic neurons in the UMAP plot of the entire dataset (Fig. 6B), these two cell types resolve into separate clusters when the input for the UMAP plot is restricted to neurons; 135 presumed multiplets were excluded from subsequent analyses.

Each cell type within the hypoxic cerebral cortex exhibits a distinctive set of up- and down-regulated transcripts as shown in the heat map in Fig. 6C. There are a small number of known hypoxia-inducible genes that exhibit common responses across multiple cell types (indicated by the horizontal arrow in Fig. 6C and shown in *SI Appendix*, Fig. S6E).

To compare transcriptome changes between the hypoxic retina and cortex at a cell type-specific level, we first defined a set of gene expression patterns in the Ndp^{KO} retina scRNA-seq dataset using CoGAPS (49) and projected these patterns into the hypoxic cortical scRNA-seq dataset (Fig. 6D). Several patterns that had high weights in specific cell types in the retina dataset had high projection weights in analogous cell types in the cortical dataset (enclosed by green lines in Fig. 6D): pattern 7 in microglia, patterns 18 and 19 in ECs, and pattern 20 in vascular smooth muscle cells and pericytes. As Muller glia exhibit distinctive transcriptome changes in the Ndp^{KO} retina (Fig. 4), it was of interest to assess the extent to which this response was
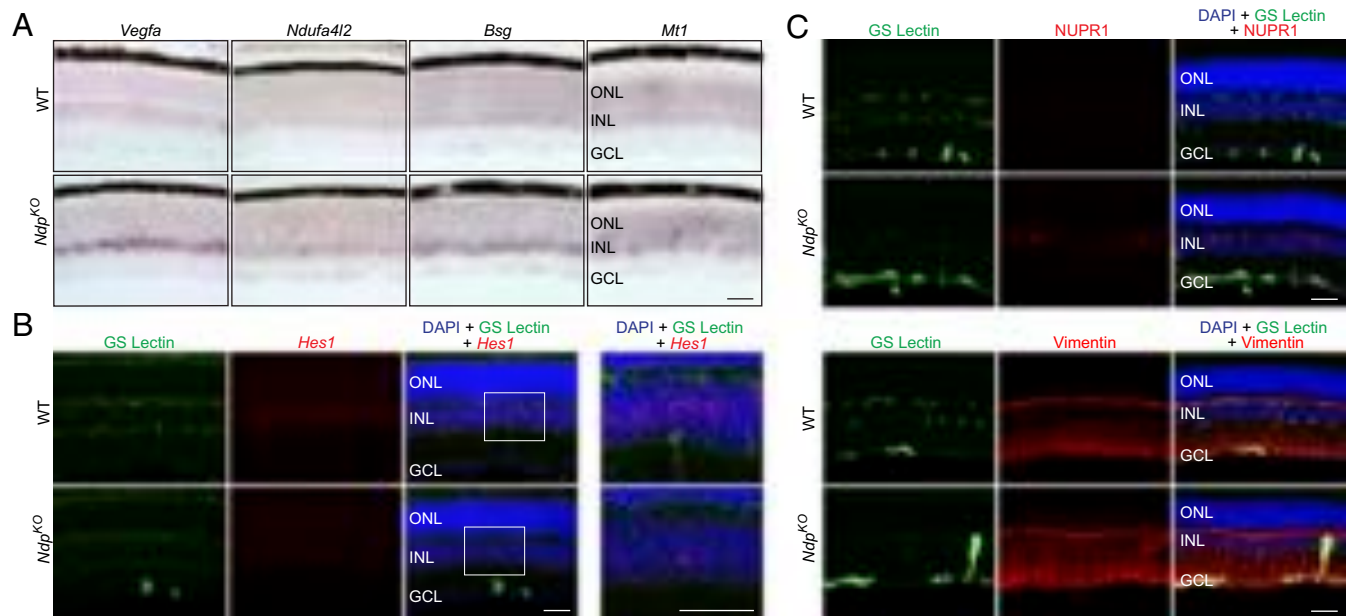
Fig. 5. Histochemical assessment of transcripts and proteins validates differentially regulated Muller glia genes in WT and Ndp^{KO} retinas. (*A*) Abundance changes for four transcripts that are up-regulated in Ndp^{KO} compared with WT retinas. In situ hybridization shows increased abundance in the INL in the Ndp^{KO} retina. (Scale bar: 50 μm.) (*B*) Fluorescent *Hes1* in situ hybridization shows decreased abundance in the INL in the Ndp^{KO} retina. The boxed region encompassing the INL is enlarged in *Right*. (Scale bars: 50 μm.) (*C*, *Upper*) Immunofluorescence of retina cross-sections showing blood vessels (GS Lectin; green), Nupr1 (red), and nuclei (DAPI; blue). NUPR1 is present in scattered Muller glial cell bodies in the Ndp^{KO} retina but is undetectable in WT retinas. (*C*, *Lower*) Immunofluorescence of retina cross-sections showing blood vessels (GS Lectin; green), Vimentin (Vim; red), and nuclei (DAPI; blue). Vimentin is modestly elevated in the Ndp^{KO} retina compared with the WT retina. GCL, ganglion cell layer; ONL, outer nuclear layer. (Scale bars: 50 μm.)

shared with one or more hypoxic cortical cell types. By CoGAPS analysis, patterns 5 and 6 most closely resembled the Muller glia-specific hypoxic response (enclosed by green lines in Fig. 6*D*). When projected onto the cortical dataset, these patterns showed the highest weights in astrocytes and oligodendrocytes.

Additional evidence for a functional relationship between Muller glia and cortical astrocytes and oligodendrocytes is seen in the heat map in Fig. 6*E*, which shows individual transcripts that are most enriched in patterns 5 and 6 (Fig. 6*D*) and that are also up-regulated by hypoxia in either cortical astrocytes or oligodendrocytes. Only a few of these genes are up-regulated in cortical neurons (Fig. 6*E*). Interestingly, *Vegfa* induction is more significant in astrocytes, oligodendrocytes, and oligodendrocyte precursor cells than in neurons (arrow in Fig. 6*E*), reminiscent of its Muller glia-specific induction in the Ndp^{KO} retina (Fig. 4*C*).

Brain Vascular EC Responses to Hypoxia. The scRNA-seq analysis of normoxic vs. hypoxic cerebral cortex presents an opportunity to explore the CNS EC-specific transcriptional changes in response to chronic tissue hypoxia. For a global assessment of transcript changes, we computed transcripts per million (TPM) from aggregated transcript abundances in either normoxic or hypoxic cortical ECs. For the identification of subtle and/or heterogenous gene expression changes, this approach is less sensitive than the differential gene expression test in Monocle2: when up- and down-regulated EC transcripts identified by Monocle2 are plotted on a TPM scatterplot, many show only small changes in TPM (*SI Appendix*, Fig. S7*A*). CNS EC-enriched transcripts (*SI Appendix*, Fig. S7*A*) [more than twofold enriched in CNS ECs relative to non-ECs (31)] and blood–brain barrier (BBB) transcripts (Fig. 7*A*) [more than twofold enriched in brain ECs relative to non-CNS ECs (31)] also show minimal differences in computed TPM between normoxic and hypoxic cortical ECs, consistent with previous observations that the BBB in cortical ECs is not disrupted in chronic hypoxia (10). To examine CNS EC subtypes, we combined published data and a recent scRNA-seq analysis of postnatal day 7 mouse brain ECs (31) to define

subsets of transcripts specifically enriched in arterial ECs, venous ECs, and tip cells. (Tip cells are the highly motile ECs at the growing front of an angiogenic vascular plexus.) Arterial and venous transcripts show little or no change in abundance between normoxic and hypoxic conditions (Fig. 7*A*, panels 2 and 3). In contrast, markers for tip cells show a clear trend toward increased abundance in hypoxic ECs relative to normoxic ECs (Fig. 7*A*, panel 4).

We next visualized the cell by cell abundances of individual arterial, venous, and tip cell transcripts in normoxic and hypoxic ECs on a UMAP plot generated using transcripts specific to each of the EC subtypes previously defined (31) (Fig. 7*B* and *SI Appendix*, Fig. S7*B*). These plots reveal the clustering of venous and arterial EC subtypes at the top and bottom, respectively, with capillary ECs in the central region. Strikingly, at the right side of the UMAP plots, there is a cluster of ECs that consistently expresses tip cell markers and is only present in the hypoxic sample. Tip cell transcripts are also more abundant among ECs in the central region of the UMAP plot (corresponding to capillary ECs) in the hypoxic sample compared with the normoxic control.

We next asked whether an up-regulation of tip cell transcripts occurs in the hypoxic retina in the context of the Ndp^{KO} retinal vasculature. As a preliminary quality control step, we first determined that an earlier analysis of Ndp^{KO} vs. WT retinal EC transcriptomes—obtained by immunoaffinity purifying retinal ECs followed by microarray hybridization (14)—had converged on the same set of differentially expressed genes defined in the scRNA-seq analysis (Fig. 7*C*, *Upper Left*). Although ECs in the hypoxic cerebral cortex and ECs in the Ndp^{KO} retina are both in close proximity to hypoxic parenchymal cells, they differ with respect to (*i*) canonical beta-catenin signaling, which is active in cortical ECs and greatly reduced in Ndp^{KO} retinal ECs, and (*ii*) the luminal blood oxygen level, which is presumably lower in the hypoxic cortical vasculature than in the normoxic Ndp^{KO} retinal vasculature. Despite these differences, the basic pattern of up-regulation of tip cell transcripts with essentially no alteration in arterial and venous transcripts is conserved between these two

Heng et al.
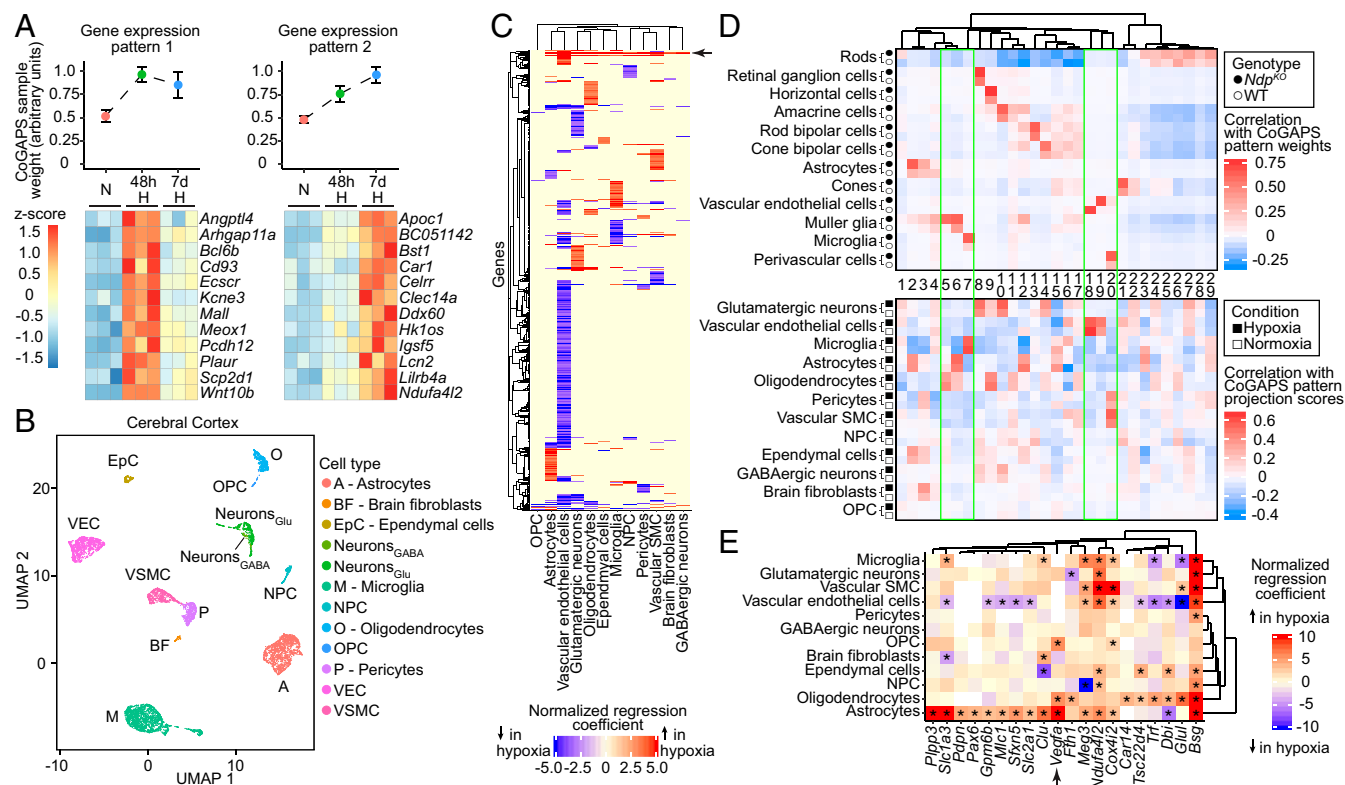
Fig. 6. Single-cell RNA-seq reveals correlated transcriptional changes between chronically hypoxic mouse cerebral cortex and *Ndp^KO* INL cell types. (*A, Upper*) Plots showing CoGAPS sample weights of whole-brain RNA-seq from mice exposed to normoxia (N), 48-h hypoxia (48 h H), and 7-d hypoxia (7 d H) for two distinct expression patterns determined by CoGAPS. Error bars represent the SEM. (*A, Lower*) Heat maps for examples of genes specific to the two CoGAPS patterns, showing gene expression (*z* score) across triplicate samples for the three experimental conditions listed above the heat maps. Each column represents a sample. (*B*) UMAP plot of scRNA-seq data from cerebral cortex from mice exposed to normoxia (control) and 7-d hypoxia. Neurons_GABA, GABAergic neurons; Neurons_Glu, glutamatergic neurons; NPC, neural progenitor cells; OPC, oligodendrocyte precursor cells; VEC, vascular endothelial cells; VSMC, vascular smooth muscle cells. (*C*) Heat map showing normalized regression coefficients for transcripts with statistically significantly differences on scRNA-seq differential gene expression analysis in cortical cell types exposed to 7-d hypoxia vs. normoxia. The arrow points to a cluster of known hypoxia-indicible genes. (*D, Upper*) Heat map showing correlation of single-cell CoGAPS pattern weights with cell type and genotype in the retina scRNA-seq dataset. (*D, Lower*) Heat map showing correlation of cortical cell type and condition with projection scores of the retinal patterns above projected into the cortical scRNA-seq dataset. Patterns are numbered sequentially according to their order in the associated dendrogram. Each pattern in the heat map *D, Upper* is aligned with its corresponding projection in the heat map in *D, Lower*. (*E*) Heat map showing, for each cortical cell type, the normalized regression coefficients for transcripts enriched in the Muller glia-associated single-cell CoGAPS patterns that are also up-regulated in astrocytes and/or oligodendrocytes from 7-d hypoxia cerebral cortices. **q* value of <0.05.

models of CNS hypoxia (Fig. 7*C*). The greater noise in the retina EC dataset compared with the cortical EC dataset likely reflects the smaller number of ECs in the retinal scRNA-seq samples.

Taken together, these analyses show that, with 1 wk of chronic hypoxia, a substantial fraction of cortical ECs is mobilized to turn on tip cell genes, presumably as part of an adaptive neoangiogenic program to increase vascular density and cerebral blood flow (5, 10). A similar conversion characterizes the *Ndp^KO* retinal vasculature and is presumably responsible for the hyperdense capillary network that develops on the vitreal face of the *Ndp^KO* retina (18), implying that the tip cell genes analyzed here can be activated in the absence of canonical Wnt signaling. It is plausible that the tip cell transcriptional program is activated in CNS ECs in response to VEGFA (55) produced by hypoxic glia in both the brain and retina.

Discussion

In this study, we have combined scRNA-seq, RiboTag sequencing, metabolic profiling and flux analysis, pharmacologic inhibition, and ultrastructural and immunohistochemical analyses to (*i*) define the response of the *Ndp^KO* retina to chronic hypoxia and (*ii*) compare the retina's hypoxia response with that of the cerebral cortex subjected to 7 d of hypoxia. For both retina and cortex, determining gene expression changes at single-cell resolution

presented a critical advantage over whole-tissue analysis, since many of the cell type-specific responses would have been difficult or impossible to detect if gene expression had been analyzed in bulk.

Metabolic Responses of the *Ndp^KO* Retina. The preservation of a nearly normal ATP level and ATP/ADP ratio in *Ndp^KO* retinas is striking, and it implies the existence of powerful homeostatic mechanisms that conserve ATP in chronic hypoxia. Since the plasma membrane Na/K-ATPase is responsible for ~50% of ATP hydrolysis in the CNS (56), we speculate that such a reduction in ATP consumption could be brought about through a reduction in Na/K-ATPase activity mediated by hypoxia-related oxidative stress-induced nonenzymatic glutathionylation and/or PKC phosphorylation (57). Such posttranslational regulation of Na/K-ATPase activity and its rapid reversal would also dynamically affect neuronal membrane potential and account for the rapidly reversible reduction in inner retinal neurotransmission in *Ndp^KO* retinas (14).

Global metabolic profiling of *Ndp^KO* retinas shows prominent metabolic changes centered around glutathione and one-carbon metabolism. Immunostaining for selected metabolites shows that some of these changes are localized to the hypoxic INL of the *Ndp^KO* retina. Similar metabolic changes have been described in hypoxic cancer cells (58). These metabolic changes mirror recent
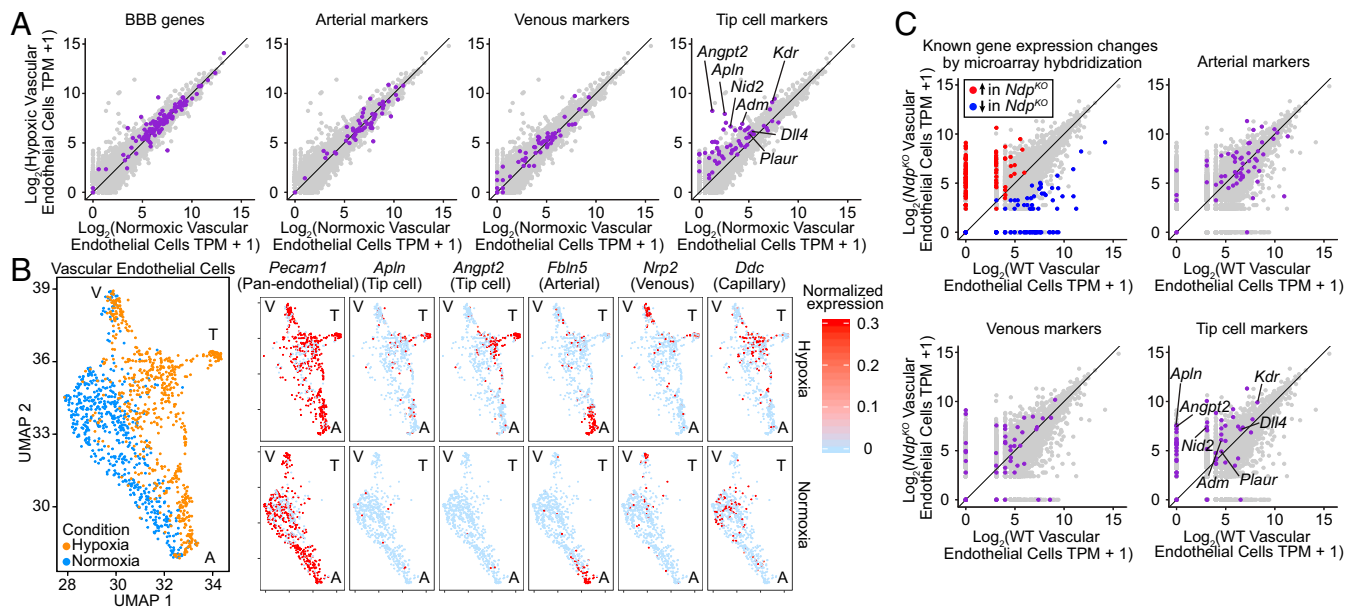
Fig. 7. Brain and retinal vascular ECs activate the tip cell transcriptional program in response to chronic tissue hypoxia. (*A*) Scatterplots showing TPM for all transcripts expressed in normoxic and/or hypoxic cortical ECs (light gray) obtained by pooling transcript counts in the cortical scRNA-seq dataset. Transcripts previously defined as enriched in BBB-type, arterial, venous, or tip cell ECs are colored purple on individual plots. A 45° line is shown in each plot. (*B, Left*) UMAP plot for hypoxic and normoxic cortical ECs. (*B, Right*) Separate plots for each transcript showing hypoxic vs. normoxic cortical ECs [based on the combined UMAP plot (*B, Left*)] color coded by the level of normalized expression for a panendothelial marker (*Pecam1*), two tip cell markers (*Apln* and *Angpt2*), an arterial marker (*Fbln5*), a venous marker (*Nrp2*), and a capillary marker (*Ddc*). A, artery; T, tip cell; V, vein. (*C*) Scatterplots as in *A* showing TPM for all transcripts expressed in WT and *Ndp^KO* retinal ECs (light gray) obtained by pooling transcript counts in the retina scRNA-seq dataset. (*C, Upper Left*) Transcripts previously shown by microarray hybridization of immunoaffinity-purified ECs to be up- or down-regulated in *Ndp^KO* compared with WT ECs are highlighted (14). (*C, Upper Right* and *Lower Right*) Transcripts previously defined as enriched in arterial, venous, or tip cell ECs are colored purple on individual plots. A 45° line is shown in each plot.

findings in mitochondrial disorders, where mitochondrial respiratory chain dysfunction leads to changes in glutathione and one-carbon metabolic pathways (59, 60). We speculate that hypoxia-induced defects in mitochondrial respiration and induction of oxidative stress in the *Ndp^KO* INL may be analogous to the metabolic adaptations in primary mitochondrial disorders.

The role of glucose-driven de novo serine synthesis in glutathione and one-carbon metabolism has been described recently (45, 59, 60). Here, we provide in vivo evidence for increased flux of glucose to serine in the *Ndp^KO* retina. This finding is especially intriguing, as it implies that cells in the *Ndp^KO* retina—despite being under energy stress due to hypoxia—divert glucose away from pyruvate production and toward the synthesis of serine, a nonessential amino acid. The importance of this pathway for cell survival in the context of chronic hypoxia is implied by our observation that inhibition of de novo serine synthesis by the PHGDH inhibitor NCT503 resulted in increased levels of cleaved Caspase-3 in the *Ndp^KO* INL but not in the WT INL.

Muller Glia, Cortical Astrocytes, and Oligodendrocytes. Muller glia, the major macroglia in the retina, exhibit a distinct gene expression profile in health (50, 54) and in disease (61). Here, we combined single-cell transcriptomics and RiboTag technology to further characterize the gene expression changes in Muller glia in *Ndp^KO* retinas. Notably, transcripts coding for NDUFA4L2, which inhibits mitochondrial Complex I, were up-regulated and enriched in *Ndp^KO* Muller glia, but they were unchanged in neurons. We also found evidence for lower Notch signaling in Muller glia as evidenced by a reduction in transcripts coding for HES1 and HES5. It is unclear if reduced Notch signaling is a specific response to hypoxia or a more generic response to cellular stress. In avian (62) and zebrafish (63) retinas, a reduction in Notch signaling in Muller glia has been linked to induction of a stem cell-like state through dedifferentiation and reentry into

the cell cycle. Mammalian Muller glia seem to have a more limited capacity for this conversion (64).

We also compared the single-cell transcriptomes of the *Ndp^KO* retina and the hypoxic cerebral cortex. Similar to the *Ndp^KO* INL, glia and neurons in the hypoxic cortex displayed distinct changes in gene expression. Compared with other cell types in the cerebral cortex, astrocytes and oligodendrocytes exhibit a transcriptional response to hypoxia that most closely resembles the response of *Ndp^KO* Muller glia. This similarity suggests similar roles for cortical and retinal glia in mitigating the hypoxic stress of surrounding neurons.

ECs in the Hypoxic CNS. The single-cell transcriptome analysis of hypoxic vs. normoxic cerebral cortex has provided a global view of the changes in EC gene expression that are associated with CNS hypoxia. This response is striking in its simplicity: capillary ECs in the hypoxic cerebral cortex activate an adaptive and previously dormant tip cell program of gene expression. We presume that this represents the gene expression correlate of the microvascular sprouting and formation of new capillaries observed by two-photon imaging in the hypoxic mouse cerebral cortex during an extended hypoxic exposure (5). In the *Ndp^KO* retina, ECs proliferate locally to form glomeruloids (18) but fail to form new intraretinal capillaries, despite the induction of the tip cell transcriptional program. Whether this failure reflects an additional requirement for beta-catenin signaling (which is absent in *Ndp^KO* retinal ECs), a nonpermissive environment for angiogenesis within the mature retina, or some combination of the two is unknown.

Clinical Relevance. This work has implications beyond the pathophysiology of Norrie disease. The observation that *Ndp^KO* retinas exhibit an increase in de novo serine biosynthesis and that INL cells in *Ndp^KO* retinas are uniquely sensitive to inhibition of that pathway may be of relevance to the pathophysiology of macular

telangiectasia (MacTel). MacTel is characterized by abnormal blood vessels in the fovea or perifoveal region, reduced capillary density in the surrounding retina (65), and loss of perifoveal Muller glia (66, 67). The disease phenotype has been modeled by genetic ablation of Muller glia in the mouse retina (68). A recent genome-wide association study of MacTel patients implicated genes involved in de novo serine biosynthesis and its associated one-carbon pathways, and it also demonstrated that serum levels of serine and glycine are decreased in MacTel cases compared with controls (69). These observations are consistent with a model in which a reduction in de novo serine synthesis and/or one-carbon metabolism renders the retina more susceptible to oxidative stress and/or hypoxia. Because complete disruption of de novo serine synthesis in $Phgdh^{-/-}$ mice leads to severe defects in CNS development (70), it would be interesting to determine whether heterozygosity for $Phgdh$ deficiency alters neuronal function or survival in models of MacTel or other CNS diseases.

This work also has implications for hypoxia tolerance in the CNS more generally. First, the reversible inactivation of neurotransmission in the Ndp^{KO} inner retina implies that, with a reduced blood supply, neurons can remain alive for months in a state of suspended animation and still recover their excitability. This natural history might account for some of the functional recovery that accompanies revascularization in the penumbra of a stroke (1). Second, the oxidative stress that accompanies hypoxia in the Ndp^{KO} INL—as inferred from the accumulation of pimonidazole and the enhanced synthesis of glutathione—supports the counterintuitive idea that reduced oxygen availability is associated with increased oxidative stress, most likely due to reduced efficiency of the electron transport chain (36). The coupling of hypoxia and oxidative stress suggests that dietary supplements that support antioxidant defenses might be broadly efficacious in patients with diverse diseases involving CNS hypoxia, including FEVR, chronic obstructive pulmonary disease, diabetic retinopathy, and cerebrovascular disease. Finally, identifying the cell type-specific changes in gene expression that are associated with chronic CNS hypoxia suggests the possibility that selective pharmacological enhancement of these gene expression programs could promote cell survival and recovery.

Materials and Methods

All animal experiments were conducted in accordance with the approved Institutional Animal Care and Use Committee protocol MO16M367 of the Johns Hopkins Medical Institutions. Mouse husbandry, single-cell isolation, scRNA-seq, RNA-seq, RiboTag experiments, in situ hybridization, immunostaining, metabolomics, in vivo ^{13}C-glucose labeling, and in vivo NCT503 experiments are described in SI Appendix.

1. Seitz RJ, Donnan GA (2015) Recovery potential after acute stroke. *Front Neurol* 6:238.
2. Tobalem S, Schutz JS, Chronopoulos A (2018) Central retinal artery occlusion–Rethinking retinal survival time. *BMC Ophthalmol* 18:101.
3. Garrido E, et al. (1996) Are Himalayan Sherpas better protected against brain damage associated with extreme altitude climbs? *Clin Sci (Lond)* 90:81–85.
4. Fan C, et al. (2016) Reversible brain abnormalities in people without signs of mountain sickness during high-altitude exposure. *Sci Rep* 6:33596.
5. Takuwa H, et al. (2013) Long-term adaptation of cerebral hemodynamic response to somatosensory stimulation during chronic hypoxia in awake mice. *J Cereb Blood Flow Metab* 33:774–779.
6. Ferrari M, et al. (2017) Hypoxia treatment reverses neurodegenerative disease in a mouse model of Leigh syndrome. *Proc Natl Acad Sci USA* 114:E4241–E4250.
7. Bickler PE, Donohoe PH (2002) Adaptive responses of vertebrate neurons to hypoxia. *J Exp Biol* 205:3579–3586.
8. Gidday JM (2006) Cerebral preconditioning and ischaemic tolerance. *Nat Rev Neurosci* 7:437–448.
9. Bernaudin M, Tang Y, Reilly M, Petit E, Sharp FR (2002) Brain genomic response following hypoxia and re-oxygenation in the neonatal rat. Identification of genes that might contribute to hypoxia-induced ischemic tolerance. *J Biol Chem* 277:39728–39738.
10. Masamoto K, et al. (2014) Microvascular sprouting, extension, and creation of new capillary connections with adaptation of the neighboring astrocytes in adult mouse cortex under chronic hypoxia. *J Cereb Blood Flow Metab* 34:325–331.
11. Gilmour DF (2015) Familial exudative vitreoretinopathy and related retinopathies. *Eye (Lond)* 29:1–14.
12. Xu Q, et al. (2004) Vascular development in the retina and inner ear: Control by Norrin and frizzled-4, a high-affinity ligand-receptor pair. *Cell* 116:883–895.
13. Junge HJ, et al. (2009) TSPAN12 regulates retinal vascular development by promoting Norrin- but not Wnt-induced FZD4/β-catenin signaling. *Cell* 139:299–311.
14. Ye X, et al. (2009) Norrin, frizzled-4, and Lrp5 signaling in endothelial cells controls a genetic program for retinal vascularization. *Cell* 139:285–298.
15. Luhmann UFO, et al. (2005) Role of the Norrie disease pseudoglioma gene in sprouting angiogenesis during development of the retinal vasculature. *Invest Ophthalmol Vis Sci* 46:3372–3382.
16. Xia C-H, et al. (2008) A model for familial exudative vitreoretinopathy caused by LPR5 mutations. *Hum Mol Genet* 17:1605–1612.
17. Chen C, et al. (2018) Optical coherence tomography angiography in familial exudative vitreoretinopathy: Clinical features and phenotype-genotype correlation. *Invest Ophthalmol Vis Sci* 59:5726–5734.
18. Rattner A, Wang Y, Zhou Y, Williams J, Nathans J (2014) The role of the hypoxia response in shaping retinal vascular development in the absence of Norrin/Frizzled4 signaling. *Invest Ophthalmol Vis Sci* 55:8614–8625.
19. Wang Y, et al. (2012) Norrin/Frizzled4 signaling in retinal vascular development and blood brain barrier plasticity. *Cell* 151:1332–1344.
20. Beck SC, et al. (2017) Long-term consequences of developmental vascular defects on retinal vessel homeostasis and function in a mouse model of Norrie disease. *PLoS One* 12:e0178753.
21. Becht E, et al. (2018) Dimensionality reduction for visualizing single-cell data using UMAP. *Nat Biotechnol* 37:38–44.
22. Beck SC, et al. (2018) Cystoid edema, neovascularization and inflammatory processes in the murine Norrin-deficient retina. *Sci Rep* 8:5970.
23. Trapnell C, et al. (2014) The dynamics and regulators of cell fate decisions are revealed by pseudotemporal ordering of single cells. *Nat Biotechnol* 32:381–386.
24. Qiu X, et al. (2017) Single-cell mRNA quantification and differential analysis with Census. *Nat Methods* 14:309–315.
25. Subramanian A, et al. (2005) Gene set enrichment analysis: A knowledge-based approach for interpreting genome-wide expression profiles. *Proc Natl Acad Sci USA* 102: 15545–15550.
26. Liberzon A, et al. (2015) The molecular signatures database (MSigDB) hallmark gene set collection. *Cell Syst* 1:417–425.
27. Wangsa-Wirawan ND, Linsenmeier RA (2003) Retinal oxygen: Fundamental and clinical aspects. *Arch Ophthalmol* 121:547–557.
28. Zhang H, et al. (2008) Mitochondrial autophagy is an HIF-1-dependent adaptive metabolic response to hypoxia. *J Biol Chem* 283:10892–10903.
29. Philp NJ, Ochrietor JD, Rudoy C, Muramatsu T, Linser PJ (2003) Loss of MCT1, MCT3, and MCT4 expression in the retinal pigment epithelium and neural retina of the 5A11/basigin-null mouse. *Invest Ophthalmol Vis Sci* 44:1305–1311.
30. Ke X, et al. (2012) Hypoxia upregulates CD147 through a combined effect of HIF-1α and Sp1 to promote glycolysis and tumor progression in epithelial solid tumors. *Carcinogenesis* 33:1598–1607.
31. Sabbagh MF, et al. (2018) Transcriptional and epigenomic landscapes of CNS and non-CNS vascular endothelial cells. *eLife* 7:e36187.
32. Moreno V, et al. (2014) An EMMPRIN-γ-catenin-Nm23 complex drives ATP production and actomyosin contractility at endothelial junctions. *J Cell Sci* 127:3768–3781.
33. Benita Y, et al. (2009) An integrative genomics approach identifies hypoxia inducible factor-1 (HIF-1)-target genes that form the core response to hypoxia. *Nucleic Acids Res* 37:4587–4602.
34. Shiota M, et al. (2008) Ets regulates peroxiredoxin1 and 5 expressions through their interaction with the high-mobility group protein B1. *Cancer Sci* 99:1950–1959.
35. Sabharwal SS, Waypa GB, Marks JD, Schumacker PT (2013) Peroxiredoxin-5 targeted to the mitochondrial intermembrane space attenuates hypoxia-induced reactive oxygen species signalling. *Biochem J* 456:337–346.
36. Semenza GL (2012) Hypoxia-inducible factors in physiology and medicine. *Cell* 148: 399–408.

NEUROSCIENCE

37. Berger SJ, et al. (1980) The distribution of the components of the cyclic GMP cycle in retina. *J Biol Chem* 255:3128–3133.
38. Chong J, et al. (2018) MetaboAnalyst 4.0: Towards more transparent and integrative metabolomics analysis. *Nucleic Acids Res* 46:W486–W494.
39. Fukuda R, et al. (2007) HIF-1 regulates cytochrome oxidase subunits to optimize efficiency of respiration in hypoxic cells. *Cell* 129:111–122.
40. Hwang HJ, et al. (2015) Hypoxia inducible factors modulate mitochondrial oxygen consumption and transcriptional regulation of nuclear-encoded electron transport chain genes. *Biochemistry* 54:3739–3748.
41. Tello D, et al. (2011) Induction of the mitochondrial NDUFA4L2 protein by HIF-1α decreases oxygen consumption by inhibiting complex I activity. *Cell Metab* 14:768–779.
42. Marc RE, Murry RF, Basinger SF (1995) Pattern recognition of amino acid signatures in retinal neurons. *J Neurosci* 15:5106–5129.
43. Marc RE, Jones BW (2002) Molecular phenotyping of retinal ganglion cells. *J Neurosci* 22:413–427.
44. Zhang T, et al. (2018) Disruption of de novo serine synthesis in müller cells induced mitochondrial dysfunction and aggravated oxidative damage. *Mol Neurobiol* 55:7025–7037.
45. Pacold ME, et al. (2016) A PHGDH inhibitor reveals coordination of serine synthesis and one-carbon unit fate. *Nat Chem Biol* 12:452–458.
46. de Melo J, et al. (2012) Injury-independent induction of reactive gliosis in retina by loss of function of the LIM homeodomain transcription factor Lhx2. *Proc Natl Acad Sci USA* 109:4657–4662.
47. Sanz E, et al. (2009) Cell-type-specific isolation of ribosome-associated mRNA from complex tissues. *Proc Natl Acad Sci USA* 106:13939–13944.
48. Fertig EJ, Ding J, Favorov AV, Parmigiani G, Ochs MF (2010) CoGAPS: An R/C++ package to identify patterns and biological process activity in transcriptomic data. *Bioinformatics* 26:2792–2793.
49. Stein-O'Brien GL, et al. (2018) Decomposing cell identity for transfer learning across cellular measurements, platforms, tissues, and species. bioRxiv:10.1101/395004.
50. Roesch K, et al. (2008) The transcriptome of retinal Müller glial cells. *J Comp Neurol* 509:225–238.
51. Miles AT, Hawksworth GM, Beattie JH, Rodilla V (2000) Induction, regulation, degradation, and biological significance of mammalian metallothioneins. *Crit Rev Biochem Mol Biol* 35:35–70.
52. Hamidi T, et al. (2012) Nupr1-aurora kinase A pathway provides protection against metabolic stress-mediated autophagic-associated cell death. *Clin Cancer Res* 18:5234–5246.
53. Verardo MR, et al. (2008) Abnormal reactivity of muller cells after retinal detachment in mice deficient in GFAP and vimentin. *Invest Ophthalmol Vis Sci* 49:3659–3665.
54. Nelson BR, et al. (2011) Genome-wide analysis of Müller glial differentiation reveals a requirement for Notch signaling in postmitotic cells to maintain the glial fate. *PLoS One* 6:e22817.
55. Blanco R, Gerhardt H (2013) VEGF and Notch in tip and stalk cell selection. *Cold Spring Harb Perspect Med* 3:a006569.
56. Howarth C, Gleeson P, Attwell D (2012) Updated energy budgets for neural computation in the neocortex and cerebellum. *J Cereb Blood Flow Metab* 32:1222–1232.
57. Fuller W, et al. (2013) Regulation of the cardiac sodium pump. *Cell Mol Life Sci* 70:1357–1380.
58. Samanta D, et al. (2016) PHGDH expression is required for mitochondrial redox homeostasis, breast cancer stem cell maintenance, and lung metastasis. *Cancer Res* 76:4430–4442.
59. Nikkanen J, et al. (2016) Mitochondrial DNA replication defects disturb cellular dNTP pools and remodel one-carbon metabolism. *Cell Metab* 23:635–648.
60. Bao XR, et al. (2016) Mitochondrial dysfunction remodels one-carbon metabolism in human cells. *eLife* 5:e10575.
61. Roesch K, Stadler MB, Cepko CL (2012) Gene expression changes within Müller glial cells in retinitis pigmentosa. *Mol Vis* 18:1197–1214.
62. Hayes S, Nelson BR, Buckingham B, Reh TA (2007) Notch signaling regulates regeneration in the avian retina. *Dev Biol* 312:300–311.
63. Sifuentes CJ, Kim J-W, Swaroop A, Raymond PA (2016) Rapid, dynamic activation of Müller glial stem cell responses in zebrafish. *Invest Ophthalmol Vis Sci* 57:5148–5160.
64. Yao K, et al. (2018) Restoration of vision after de novo genesis of rod photoreceptors in mammalian retinas. *Nature* 560:484–488.
65. Chidambara L, et al. (2016) Characteristics and quantification of vascular changes in macular telangiectasia type 2 on optical coherence tomography angiography. *Br J Ophthalmol* 100:1482–1488.
66. Powner MB, et al. (2010) Perifoveal müller cell depletion in a case of macular telangiectasia type 2. *Ophthalmology* 117:2407–2416.
67. Len ACL, et al. (2012) Pilot application of iTRAQ to the retinal disease macular telangiectasia. *J Proteome Res* 11:537–553.
68. Chung SH, et al. (2013) Differential gene expression profiling after conditional Müller-cell ablation in a novel transgenic model. *Invest Ophthalmol Vis Sci* 54:2142–2152.
69. Scerri TS, et al.; MacTel Project Consortium (2017) Genome-wide analyses identify common variants associated with macular telangiectasia type 2. *Nat Genet* 49:559–567.
70. Yoshida K, et al. (2004) Targeted disruption of the mouse 3-phosphoglycerate dehydrogenase gene causes severe neurodevelopmental defects and results in embryonic lethality. *J Biol Chem* 279:3573–3577.